Revisiting the Impact of Tungsten on the Catalytic Properties of Ammonia-SCR V2O5-WO3/TiO2 Catalysts: Geometric vs. Electronic Effects

Hermann Wilfried Siaka, Christophe Dujardin, Alain Moissette, Pascal Granger

chemistry

MDPI

Article

Revisiting the Impact of Tungsten on the Catalytic Properties of Ammonia-SCR V_2O_5-WO_3/TiO_2 Catalysts: Geometric vs. Electronic Effects

Hermann Wilfried Siaka [1], Christophe Dujardin [1], Alain Moissette [2] and Pascal Granger [1,*]

[1] Univ. Lille, CNRS, Centrale Lille, Univ. Artois, UMR 8181—UCCS—Unité de Catalyse et Chimie du Solide, 59000 Lille, France
[2] Laboratoire de Spectroscopie pour les Interactions la Réactivité et l'Environnement, Univ. Lille, CNRS, UMR CNRS 8516-LASIRE, 59000 Lille, France
* Correspondence: pascal.granger@univ-lille.fr; Tel.: +33-3-20-43-49-38

Abstract: The SCR performance of V_2O_5-WO_3/TiO_2 SCR-catalysts characterized by different surface W density (2.1W/nm^2 and 9.5W/nm^2) and different surface V density varying in the range 1–8V/nm^2 has been investigated in order to clarify existing controversies on the preferential involvement of electronic and geometric effects in the catalytic properties. It was found that tungsten has a weak effect on the VO_x cluster size distribution through contraction of dilution effect. In contrast, the optimal interaction between W and V, when both reach their highest composition, appears to be a relevant parameter that can enhance their acidic properties and improve the catalytic efficiency in dry conditions. On the other hand, an absence of significant interaction leads to discontinuity due to deactivation. In the presence of steam, acidic properties are averaged, lowering the impact of the V to W ratio. Finally, the critical importance of acidic properties which outperform redox properties in the definition of active site is pointed out in the light of this study.

Keywords: selective catalytic reduction; NO_x; NH_3; V_2O_5-WO_3/TiO_2

Citation: Siaka, H.W.; Dujardin, C.; Moissette, A.; Granger, P. Revisiting the Impact of Tungsten on the Catalytic Properties of Ammonia-SCR V_2O_5-WO_3/TiO_2 Catalysts: Geometric vs. Electronic Effects. *Chemistry* **2023**, *5*, 294–313. https://doi.org/10.3390/chemistry5010023

Academic Editors: José Antonio Odriozola and Hermenegildo García

Received: 27 January 2023
Revised: 15 February 2023
Accepted: 16 February 2023
Published: 20 February 2023

1. Introduction

The selective catalytic reduction (SCR) of NO_x by ammonia over V_2O_5-WO_3/TiO_2 catalysts can be considered as a consolidated after-treatment technology. Indeed, NO_x are selectively reduced into nitrogen in a broad operating window, both at the lab scale and under relevant industrial conditions [1–4]. V_2O_5-WO_3/TiO_2 catalysts are recognized for their remarkable selectivity, delaying the undesired ammonia oxidation in the presence of a large excess of oxygen. This catalytic technology was originally suited for after-treatment of tail gas of stationary sources. Industrial furnaces of glass factories are concerned with the equivalent of 2.5 kg NO_x emitted per ton of glass bottle produced [5].

Surprisingly, a renewed interest is perceptible, likely due to extended applications in the field of postcombustion catalysis [6–8], for which particular attention should be paid to detrimental poisoning effects and thermal sintering. It was found that the addition of tungsten to vanadium provides significant improvements in catalytic performances related to acidity enhancement, stabilization of well-dispersed active vanadate species, slower growth of non-selective V_2O_5 aggregates, as well as improved resistance to alkali poisoning, as key points for mobile applications [4,9,10]. Despite extensive practical developments and huge efforts to identify the functionalities that govern the kinetic behavior of these SCR catalysts, some controversies persist because of complex interactions between tungsten and vanadium. Alemany et al. [11] reported that ternary V_2O_5-WO_3/TiO_2 systems outperform the intrinsic catalytic properties of binary V_2O_5/TiO_2 and WO_3/TiO_2 systems which reflect synergy effects on the reaction rate assigned to peculiar electronic interactions between V and W. These authors suggested that these electronic effects cause improved reducibility.

Nevertheless, the influence of geometric effects can be also suggested if tungsten acts as diluent, improving the resistance of the active vanadate species to thermal sintering. The debate is still active, and the relative contributions of these effects is usually difficult to distinguish. Indeed, surface instabilities under reaction conditions and related surface reconstructions, induced by poisoning and/or thermal sintering, make it more complex to achieve a better understanding of the specificity of tungsten and vanadia in the construction of the active sites. In short, a dual-site reaction mechanism characterizes ammonia-SCR on V_2O_5-WO_3/TiO_2 catalysts, coupling redox and acidic behavior to adsorb ammonia and reduce NO_x into N_2 according to an Eley–Rideal reaction mechanism [1,12]. Optimal $DeNO_x$ activity would require a pair of sites combining a redox site and a nearest-neighbor non-reducible site [3].

Among the wide variety of NH_3-SCR catalysts investigated to date, e.g., bulk and supported V-based systems, a clear identification of the composition and the stoichiometry of redox and acid sites is subjected to discussion. At first glance, there is a relative consensus for redox sites assigned to polyvanadate, but for acid sites, more complex assignments come from the coexistence of VO_x and WO_x species. In the particular case of bulk binary $CeVO_4$ systems, a dual-site mechanism has been suggested, involving the participation of V-O-V bridged at the vicinity of V-O-Ce sites [13]. On the other hand, the involvement of VO_x and WO_x entities acting as an acid site on $CeV_{1-x}W_xO_4$ is also discussed [14]. Nonetheless, more insights are needed to achieve improved optimization to properly control electronic or geometric interactions between W and V, in order to magnify acidic and redox properties of vanadate species.

There was also an important debate in the late 1990s about the chemical nature of acid sites and their related strength, e.g., Lewis vs. Brønsted acid sites [6]. Brønsted acid sites were initially renowned as the main factor acting in the catalytic properties; more recently, time-resolved spectroscopic measurements pointed out the prevalence of Lewis acid sites on vanadate species [7]. The role of tungsten remains unclear. Indeed, Kompio et al. found that dimeric vanadate species mostly contribute to the catalytic performance of V_2O_5-WO_3/TiO_2 [15]. These authors found a beneficial effect due to the formation of a more active V-O-V structure than in isolated vanadates, thanks to the segregation of tunsgtate species leading to optimum size for vanadate aggregates. Nonetheless, they did not rule out the hypothesis that a direct effect could also influence the catalytic activity of vanadates. Prominent structural effects have also been found from ^{51}V MAS analysis. Jaegers et al. [16] highlighted the promoter role of W in inducing structural effects instead of electronic effects, as was earlier suggested.

This paper will contribute to this debate based on a study which accounts for the impact of high and low tungsten loadings in V_2O_5-WO_3/TiO_2 SCR-catalysts in order to check hypothetical geometrical effects assigned to dilution or, conversely, contraction effects of WO_x on VO_x species. Accordingly, redispersion or, conversely, aggregation process of monomeric into polymeric vanadate species can be envisioned. Particular attention has been paid to the extent of such processes at various surface VO_x densities and their related impact on their catalytic properties. It will be suggested that their catalytic behavior cannot be uniformly explained according to the tungsten loading and can also strongly depend on the composition of the inlet gas mixture, e.g., dry vs. wet conditions. Indeed, as reported elsewhere, the creation of new Brønsted acid sites from the hydrolysis of molecularly dispersed vanadia species can potentially change the catalytic efficiency of NH_3-SCR catalysts [17].

2. Experimental

2.1. Catalysts Preparation

V_2O_5-WO_3/TiO_2 were prepared by successive impregnation of TiO_2-P25 (93 m^2/g), supplied by Degussa. Prior to impregnation, TiO_2 was washed, dried and calcined at 500 °C in air. It was verified that these treatments did not significantly alter the porosity and the structural properties of the support materials preserving the anatase structure. Successive

impregnations were carried out, respectively, from aqueous solution obtained from the dissolution of ammonium metatungstate and ammonium metavanadate. In the latter case, oxalic acid (2 mol/L) was added to improve the dispersion. Impregnation was performed in excess of solvent with appropriate amounts of tungsten and vanadium to prepare two series characterized by the following surface tungsten density values: 2.1W/nm^2 and 9.5W/nm^2. For each series, corresponding amounts of vanadium led to surface density of 1V/nm^2, 4V/nm^2 and 8V/nm^2. The impregnated precursors, after vanadium impregnation, were successively dried in air at 100 °C overnight and calcined at 450 °C in air for 4 h. The calcined samples were respectively labeled ${}_yW_xV$, where x and y respectively represent the surface density of vanadium and tungsten. Catalyst composition and corresponding nomenclature are reported in Table 1.

Table 1. Nomenclature and composition from X-ray fluorescence analysis of V_2O_5-WO_3/TiO_2 catalysts.

Nomenclature	Composition (wt.%)	
	W	V
2.1W-1V	5.5	2.0
2.1W-4V	5.5	7.8
2.1W-8V	5.5	14.8
9.5W-1V	21.0	1.7
9.5W-4V	21.0	6.5
9.5W-8V	21.0	12.5

2.2. Physicochemical Characterization

The elemental composition of the catalysts was determined using a Bruker S2 Ranger type fluorescence spectrometer equipped with a palladium X-ray tube and an energy dispersion detector. The measurements were carried out under air on catalysts in powder form. XRD analysis was carried out on a Bruker AXS D8 Advance diffractometer operating in Bragg–Brentano geometry. The experimental parameters were the following: Cu Kα radiation (λ = 0.154 nm), 2θ range of 20–80°, steps of 0.02° and dwell time 0.5 s/step. Raman spectroscopic measurements were performed on a Raman micro-spectrometer Xplora Plus (Horiba Scientific, Kyoto, Japan) equipped with Syncerity CCD detector. Spectra were recorded by using an excitation wavelength of 638 nm. Scanning electron microscopy (SEM) and energy-dispersive X-ray spectroscopy (EDS) analyses were performed on a Jeol JSM-7800F (JEOL Ltd., Tokyo, Japan) working at voltage acceleration of 15 kV with a resolution of 1.5 nm. The reducibility of WO_x and VO_x species was investigated from H_2 temperature-programmed reduction experiments (H_2-TPR) on a Micromeritics Autochem II 2920 analyzer (Micromeritics, Norcross, GA, USA). Samples were exposed to a flow of 5 vol.% H_2 in Ar with a temperature gradient of 10 °C/min. UV-vis spectra were recorded on a Perkin Elmer spectrometer Lambda 650s (PerkinElmer, Waltham, MA, USA). Diffuse Reflectance spectra were recorded in the wavelength range 200–900 nm with a step of 0.2 nm.

Specific surface area was measured by nitrogen physisorption at −196 °C with a TriStar II (Micromeritics) analyzer. Prior to physisorption measurements, powder samples were outgassed at 120 °C for 10 h under primary vacuum. Specific surface areas were calculated according to the Brunauer–Emmett–Teller (BET) theory. Temperature-programmed desorption of ammonia (NH_3-TPD) experiments were performed on 100 mg catalyst from 120 °C to 700 °C on a Micromeritics Autochem II 2920 analyzer. The outlet gas mixture was analyzed by an Omnistar Balzers Mass Spectrometer (Pfeiffer Vacuum, Aßlar, Germany) to withdraw the contribution of water and the weak formation of NO_x coming from the oxidation of adsorbed ammonia at high temperature. Prior to ammonia adsorption at 120 °C, the samples were degassed in He at the same temperature. Pre-adsorbed samples were evacuated under He flow to remove physisorbed ammonia. Infrared spectroscopic measurements during pyridine adsorption-desorption experiments were carried out on a Nicolet Protégé 460 infrared spectrometer (ThermoFisher Scientific, Waltham, MA, USA).

Samples were preheated under vacuum (10^{-5} mbar) at 450 °C. After cooling down at room temperature (RT), they were exposed to 1 Torr pyridine until saturation coverage and then evacuated at different temperatures in the range 150–350 °C. The respective values of the absorption coefficients used for the quantification of Lewis (L) and Brønsted (B) acid sites after integration of infrared bands were 2.22 cm.µmol^{-1} and 1.67 cm.µmol^{-1}, as determined from previous calibrations.

2.3. Kinetic Measurements

Catalytic measurements were performed at atmospheric pressure in a fixed-bed flow reactor. 200 mg catalyst in powder form with an average grain size of 200 µm was diluted with 800 mg SiC. The inlet reaction mixture was composed of 400 ppm NH_3, 400 ppm NO and 8 vol.% O_2 balanced with helium in the presence or in the absence of 10 vol.% H_2O. The total flow rate was adjusted to 15 L.h^{-1}, corresponding to a gas hourly space velocity of 75,000 mL.h^{-1}.g^{-1}. The catalytic performances were evaluated from temperature-programmed reaction (TPR) experiments in the temperature range 100–450 °C at a constant heating rate of 2 °C.min^{-1}. Steady-state reaction rate measurements were carried out at 160 °C according to the protocol described in Figure 1 and Table 1. The composition of the outlet gas mixture was monitored by a μGC for N_2 and N_2O and by a chemiluminescence analyzer for NO_x. Prior to catalytic experiments, the samples were heated overnight at 450 °C in a flow of 20 vol.% O_2.

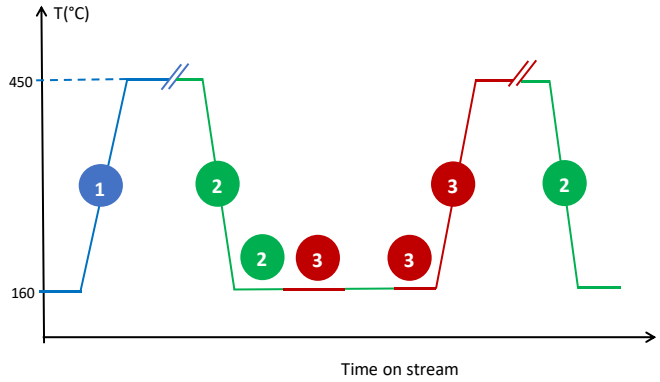

Figure 1. Protocol used for temperature-programmed and steady-state rate measurements.

Transient and steady-state catalytic experiments were performed according to the protocol described in Figure 1. NO_x conversion and selectivity towards N_2 production were recorded in different inlet feed gas mixture compositions, specified in Table 2, in the presence (wet conditions) or in the absence of steam (dry conditions).

Table 2. Composition of the inlet reaction mixtures during transient and steady-state experiments according to the protocol described in Figure 1.

ID Experiment	NO_x (ppm)	NH_3 (ppm)	O_2 (%)	H_2O (%)
1	-	-	20	-
2	400	400	8	-
3	400	400	8	10

3. Results

Catalytic performances were typically evaluated in standard operating conditions corresponding to Equation (1). The reoxidation of V^{4+} to V^{5+} during the catalytic cycle is recognized as the slow step. The standard SCR reaction competes with the parasitic ammonia oxidation according to Equations (2) and (3), which predominantly occurs at

high temperature. As a consequence, a typical volcano-type curve is observed for the NO_x conversion profile vs. temperature, reflecting the aforementioned catalytic behavior.

$$2NO + 2NH_3 + 1/2O_2 = 2N_2 + 3H_2O \quad (1)$$

$$2NH_3 + 5/2O_2 = 2NO + 3H_2O \quad (2)$$

$$2NH_3 + 2O_2 = N_2O + 3H_2O \quad (3)$$

3.1. Performance of NH_3-SCR Catalysts in Standard Conditions from Temperature-Programmed Reaction (TPR) Experiments

Conversion and selectivity profiles vs. temperature are illustrated in Figures 2 and 3. First, in the absence of vanadium, the catalytic efficiency of 2.1W and 9.5W is restricted to high temperature, e.g., above 400 °C. As expected, sharp enhancement in NO_x conversion arises below 300 °C after V incorporation, irrespective of the inlet mixture composition, e.g., dry or wet conditions. NO_x is quantitatively reduced into nitrogen as unique reaction product up to 350 °C. At first glance, the catalytic behavior of 2.1W-*x*V and 9.5W-*x*V does not differ significantly in dry conditions, emphasizing a gain in conversion with a rise in V content. In contrast, a loss of conversion operates at the highest V density. This behavior seems in agreement with previous investigations concluding on the polymerization of less-active isolated VO_x species into more active metavanadate species. The loss of conversion markedly observed on highly loaded vanadium samples is generally explained by the presence of less selective polymeric vanadate species and/or V_2O_5 aggregates favoring the parasitic ammonia oxidation into NO. The formation of unselective polyvanadates species also has a detrimental effect on the product distribution with a joint production of N_2O. It is worthwhile to note that steam has a beneficial impact at high temperature, suppressing ammonia oxidation and then restoring a remarkably high selectivity in NO_x reduction into nitrogen. Let us note that this peculiar behavior does not seem directly related to W content as the same trends characterize 2.1W-*x*V and 9.5W-*x*V for $x \geq 4$.

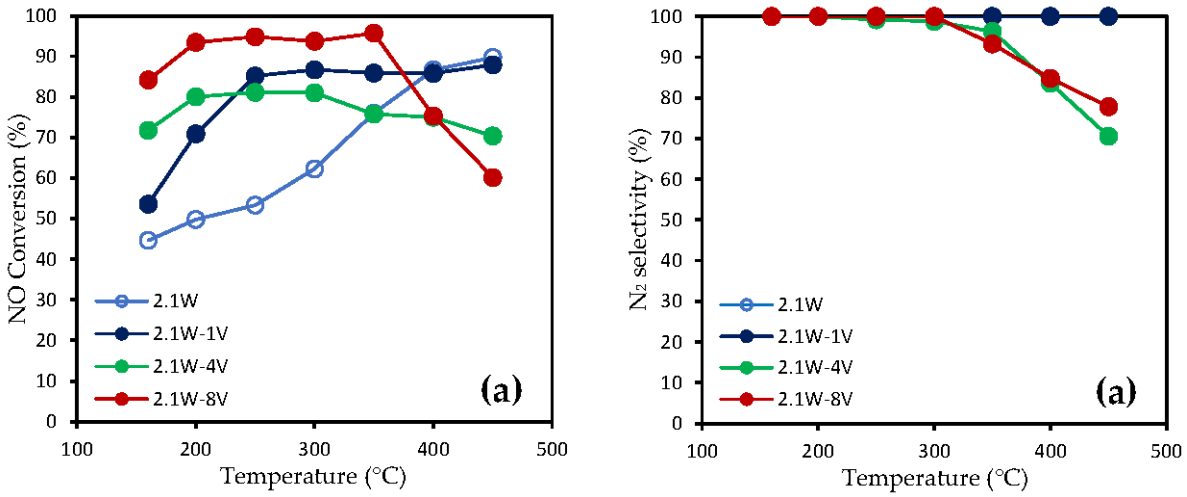

Figure 2. *Cont.*

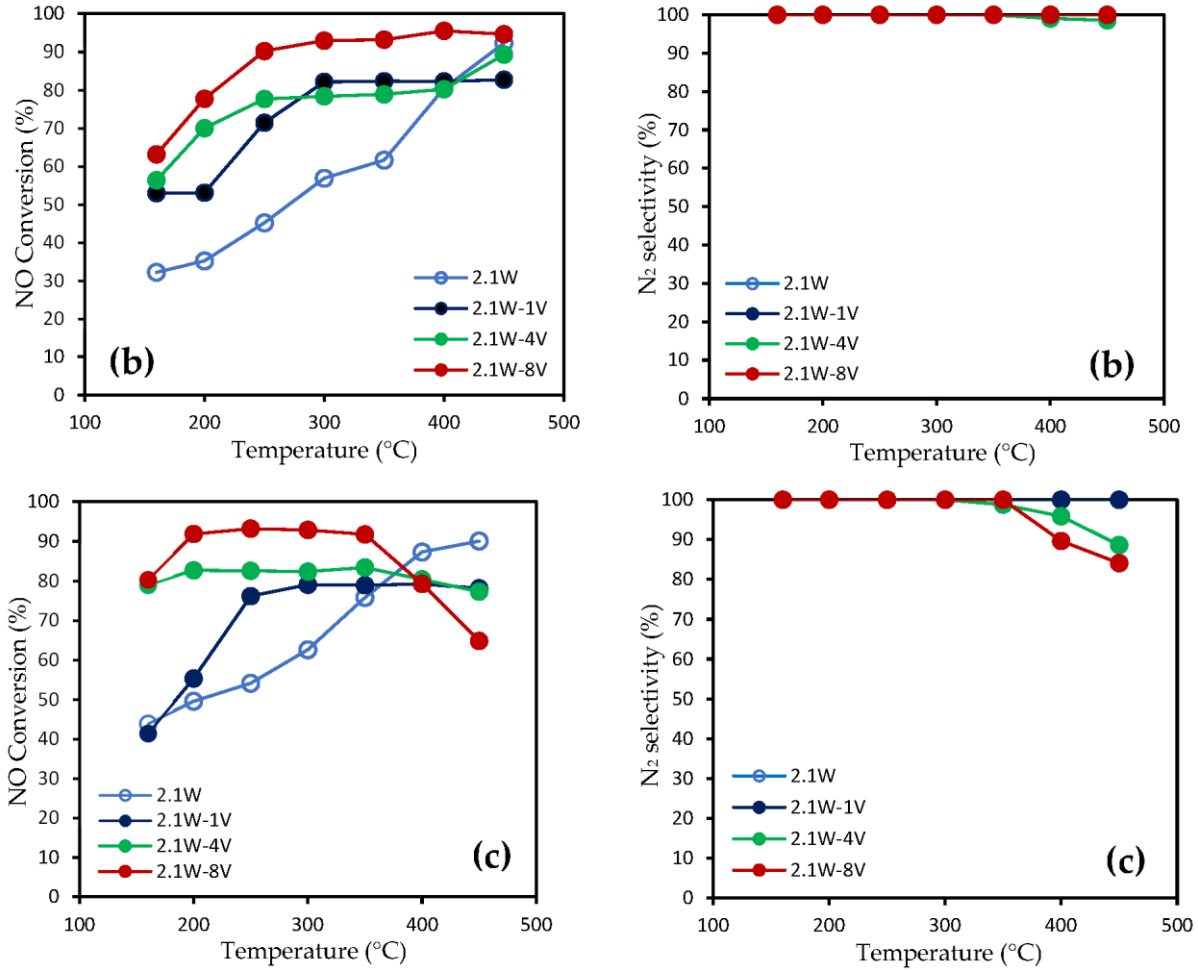

Figure 2. Conversion and N_2 selectivity profiles vs. temperature recorded on 2.1W-*x*V during ammonia SCR: (**a**) Dry ID 2 operating conditions on preheated freshly prepared samples; (**b**) Wet conditions ID 3; (**c**) Dry conditions ID 2 on samples exposed to wet conditions according to ID3. Gas hourly space velocity of 75,000 $mL.h^{-1}.g^{-1}$.

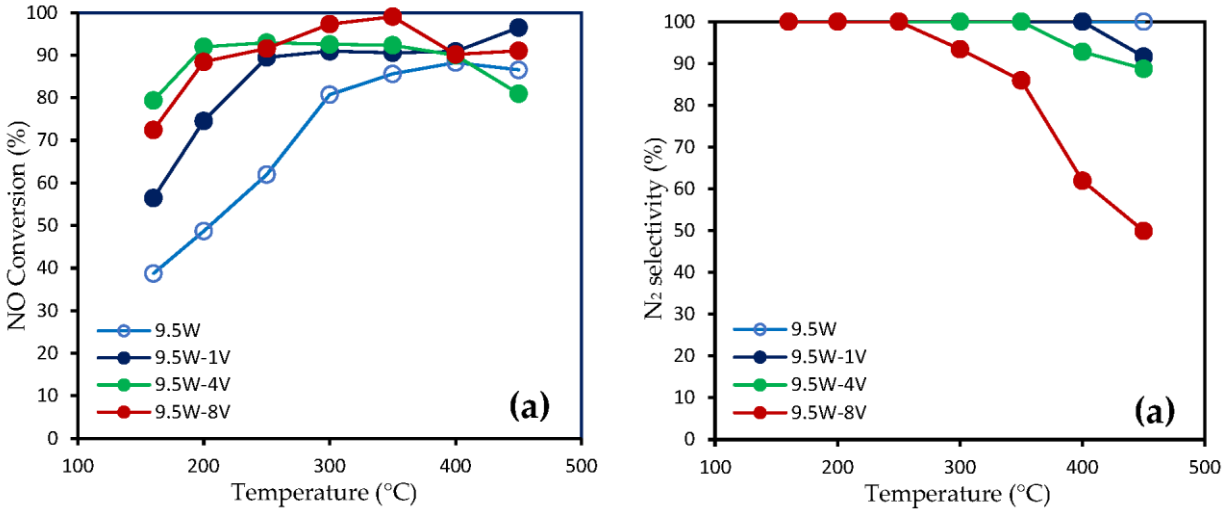

Figure 3. *Cont.*

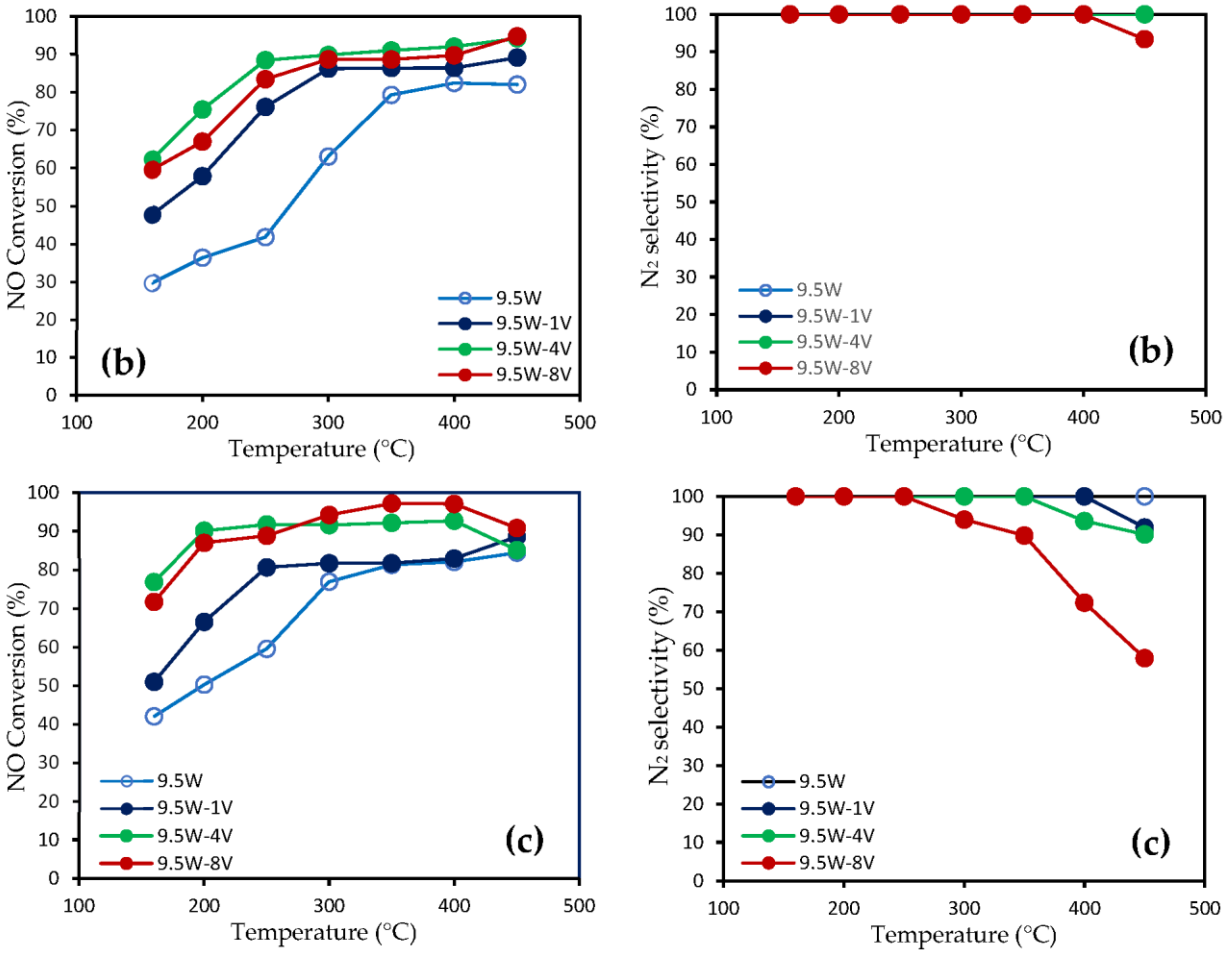

Figure 3. Conversion and N_2 selectivity profiles vs. temperature recorded on 9.5W-*x*V during ammonia SCR: (**a**) Dry ID 2 operating conditions on preheated freshly prepared samples; (**b**) Wet conditions ID 3; (**c**) Dry conditions ID 2 on samples exposed to wet conditions according to ID3. Gas hourly space velocity of 75,000 $mL.h^{-1}.g^{-1}$.

3.2. Steady-State Rate Measurements on V_2O_5-WO_3/TiO_2 at 160 °C for the Standard NH_3-SCR

In short, the power-law rate expression as a function of the rate constant k and reactant concentrations in Equation (4), where α, β and γ stand for the reaction orders with respect to NO, NH_3 and O_2, respectively, can be simplified. In a large excess of oxygen and below 300 °C, α~1 and β~0 are often observed, which reflects a strong ammonia adsorption [18–20]. In contrast, NO adsorbs weakly on vanadia surface [19]. Hence, first-order kinetics can be postulated which typically reflect an Eley–Rideal reaction mechanism with reaction rate *r* modeled based on a plug flow reactor mass balance, in agreement with Equations (5) and (6) where *W*, F_0, $[NO_x]_0$ and X_{NOx} are, respectively, the weight sample of catalyst, the total volumetric flow rate, the inlet molar concentration of NO and the conversion of NO_x.

$$r = k[NO]^{\alpha}[NH_3]^{\beta}[O_2]^{\gamma} \quad (4)$$

$$k = \frac{F_0}{W} \ln \frac{1}{1 - X_{NOx}} \quad \left(\mathrm{L\,s^{-1}g^{-1}}\right) \quad (5)$$

$$r = k[NO_x]_0(1 - X_{NOx}) = \frac{F_{NO_{x,inlet}}}{W}(1 - X_{NOx}) \ln \frac{1}{1 - X_{NOx}} \left(\mathrm{mol\,s^{-1}g^{-1}}\right) \quad (6)$$

Steady-state rate measurements were performed at 160 °C. According to the level of NO_x conversions, the occurrence of mass transfer phenomena was verified through the calculation of the Weisz–Prater criterion given by Equation (7), where r_{obs} is the measured reac-

tion rate expressed in mol.m^3.s^{-1}, C_{obs} is the steady-state concentration in mol.m^{-3}, $D_{eff,NO}$ is the NO effective diffusivity expressed in m^2.s^{-1} in the range 1.0–1.5 × 10^{-6} m.s^{-1} [21] and L = d_p/6 is the volume-to-surface ratio of the grain in m. It was found that rate measurements led to values lower than 10^{-2}, which fulfilled the boundary conditions given by Equation (7) and suggested the prevalence of a kinetic regime [22].

$$\frac{r_{obs}L^2}{C_{obs}D_{eff,NO}} < 1 \quad (7)$$

Normalized reaction rates expressed per square meter, calculated for pre-activated 2.1W-*x*V and 9.5W-*x*V catalysts and after exposure to wet conditions, are reported in Tables 3 and 4. Obviously, no deviation is noticeable due to an alteration of the surface exposed to steam at 450 °C, which emphasizes a rather good stability of vanadate species segregated onto the surface and being relatively resistant to sintering process in these operating conditions. This trend has been also confirmed at high temperature in the TPR conversion profiles with the absence of deterioration of the catalyst selectivity due to the occurrence of the oxidation reaction of ammonia. During steady-state rate measurements in the presence of 10 vol.% H_2O, water inhibition is only observed on 2.1W and 9.5W. In contrast, 2.1W-*x*V and 9.5W-*x*V do not seem sensitive to this detrimental effect at low temperature.

Table 3. Rate measurements during ammonia-SCR on 2.1W-*x*V catalyst at 160 °C.

Catalyst	Reactive Exposure	X_{NO}	*k* (L.mol^{-1}s^{-1})	Specific Rate *r* (µmol.g^{-1}s^{-1})	Normalized Rate (µmol.s^{-1}.m^{-2})
2.1W	dry conditions [a]	0.45	1.23 × 10^{-2}	0.11	1.86 × 10^{-3}
	wet conditions [b]	0.32	0.81 × 10^{-2}	0.09	1.50 × 10^{-3}
	dry conditions [c]	0.44	1.20 × 10^{-2}	0.11	
2.1W-1V	dry conditions [a]	0.54	1.60 × 10^{-2}	0.12	2.06 × 10^{-3}
	wet conditions [b]	0.53	1.57 × 10^{-2}	0.12	2.05 × 10^{-3}
	dry conditions [c]	0.41	1.11 × 10^{-2}	0.11	
2.1W-4V	dry conditions [a]	0.72	2.64 × 10^{-2}	0.12	2.30 × 10^{-3}
	wet conditions [b]	0.56	1.72 × 10^{-2}	0.12	2.33 × 10^{-3}
	dry conditions [c]	0.79	3.25 × 10^{-2}	0.11	
2.1W-8V	dry conditions [a]	0.84	3.84 × 10^{-2}	0.10	1.95 × 10^{-3}
	wet conditions [b]	0.63	2.08 × 10^{-2}	0.13	2.46 × 10^{-3}
	dry conditions [c]	0.80	3.38 × 10^{-2}	0.11	

[a] 400 ppm NO_x, 400 ppm NH_3 and 8 vol.% O_2 on calcined samples; [b] 400 ppm NO_x, 400 ppm NH_3, 8 vol.% O_2 and 10 vol.% H_2O on calcined samples; [c] 400 ppm NO_x, 400 ppm NH_3 and 8 vol.% O_2 after testing in wet conditions.

Table 4. Rate measurements during ammonia-SCR on 9.5W-*x*V catalyst at 160 °C.

Catalyst	Reactive Exposure	X_{NO}	*k* (L.mol^{-1}.s^{-1})	Specific Rate *r* (µmol.g^{-1}.s^{-1})	Normalized Rate (µmol.s^{-1}.m^{-2})
9.5W	dry conditions [a]	0.39	1.02 × 10^{-2}	0.10	1.97 × 10^{-3}
	wet conditions [b]	0.30	0.73 × 10^{-2}	0.08	1.62 × 10^{-3}
	dry conditions [c]	0.42	1.13 × 10^{-2}	0.11	
9.5W-1V	dry conditions [a]	0.56	1.73 × 10^{-2}	0.12	2.58 × 10^{-3}
	wet conditions [b]	0.48	1.35 × 10^{-2}	0.12	2.41 × 10^{-3}
	dry conditions [c]	0.51	1.48 × 10^{-2}	0.12	
9.5W-4V	dry conditions [a]	0.79	3.29 × 10^{-2}	0.11	2.93 × 10^{-3}
	wet conditions [b]	0.62	2.03 × 10^{-2}	0.13	3.31 × 10^{-3}
	dry conditions [c]	0.77	3.04 × 10^{-2}	0.12	
9.5W-8V	dry conditions [a]	0.72	2.68 × 10^{-2}	0.12	3.57 × 10^{-3}
	wet conditions [b]	0.60	1.88 × 10^{-2}	0.13	3.68 × 10^{-3}
	dry conditions [c]	0.72	2.62 × 10^{-2}	0.12	

[a] 400 ppm NO_x, 400 ppm NH_3 and 8 vol.% O_2 on calcined sample; [b] 400 ppm NO_x, 400 ppm NH_3, 8 vol.% O_2 and 10 vol.% H_2O on calcined sample; [c] 400 ppm NO_x, 400 ppm NH_3 and 8 vol.% O_2 after testing in wet conditions.

Particular attention has been paid to the effect of vanadium loading on normalized reaction rates on 2.1W-*x*V and 9.5W-*x*V, respectively, in dry and wet conditions (see Figure 4). A volcano-type curve characterizes the evolution of the normalized reaction rate vs. the vanadium density on 2.1W-*x*V in dry conditions. In contrast, this trend is not reproduced on 9.5W-*x*V, for which a gradual increase is observed. Let us note that in wet conditions (see Figure 4b), the behavior is not drastically modified. Nonetheless, it must be emphasized that the apparent maximum appearing in dry conditions near 4 V. at./nm^2 on 2.1W-*x*V is no longer observed in wet conditions. Such differences raise questions about the effective role of tungsten at increasing loading. Indeed, tungsten could induce a beneficial dilution effect on 9.5W-*x*V in order to achieve optimal size for VO_x aggregates, while at low W content, coalescence of VO_x species into less selective polymeric species would no longer be prevented. Alternately, the nature of interaction between V and W could differ on both series, inducing changes in the adsorptive properties of VO_x species, e.g., the strength of ammonia adsorption thanks to the close proximity of V and W. Finally, the negative impact of water observed on bare V samples disappears after vanadium incorporation. A slight beneficial effect is even observed on 2.1W-*x*V and 9.5W-*x*V for $x \geq 4$, which could suggest a preferential involvement of VO_x acid sites.

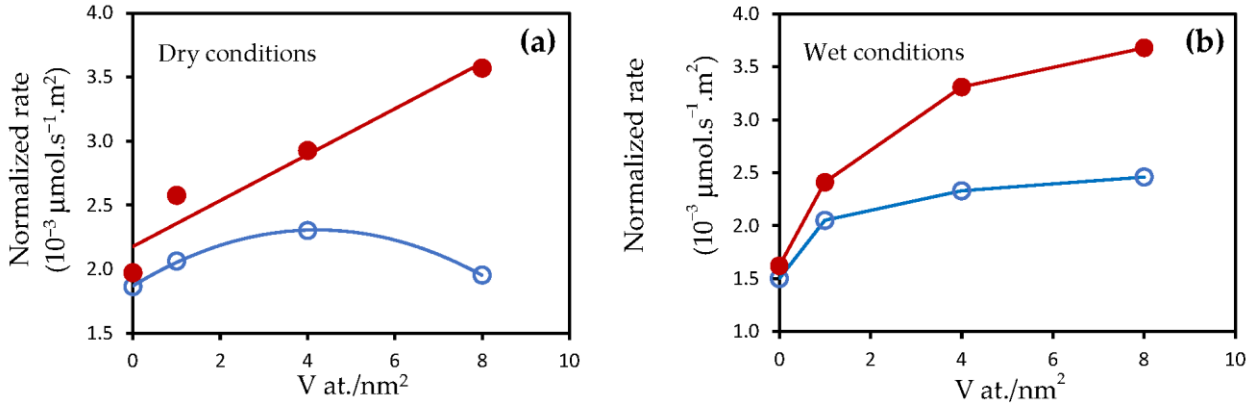

Figure 4. Vanadium density and relative concentration of vanadium dependencies of the normalized reaction rate of 2.1W-*x*V (○) and 9.5W-*x*V (●) in ammonia-SCR: 400 ppm NO, 400 ppm NH_3, 8 vol.% O_2 in the presence (wet conditions) or in the absence (dry conditions) of 10 vol.% H_2O: (**a**) dry conditions; (**b**) wet conditions.

3.3. Bulk Physicochemical Properties of Supported V_2O_5-WO_3/TiO_2 Catalysts: Structural vs. Reducibility

3.3.1. Bulk Structure and Reducibility of Vanadate and Tungstate Species

XRD patterns on low tungsten loaded samples, e.g., 2.1W*x*V with x = 1, 4 and 8, in Figure 5 only reveal the anatase TiO_2 phase (PDF 00-021-1271). In contrast, additional weak reflections appear distinctly at 2θ = 23.71°, 28.77°, 33.64° and 41.52° on XRD patterns recorded on the series 9.5W*x*V assigned to WO_3 agglomerates (PDF 00-020-1324). Let us note that even at high vanadium content, no discernible reflection can be attributed to bulk V_2O_5. Scanning electron microscopy coupled with EDS analysis confirms homogeneous distribution of vanadate species irrespective of W content. On the other hand, heterogeneities in composition appear on highly loaded W samples in agreement with XRD observations corresponding to large WO_x aggregates.

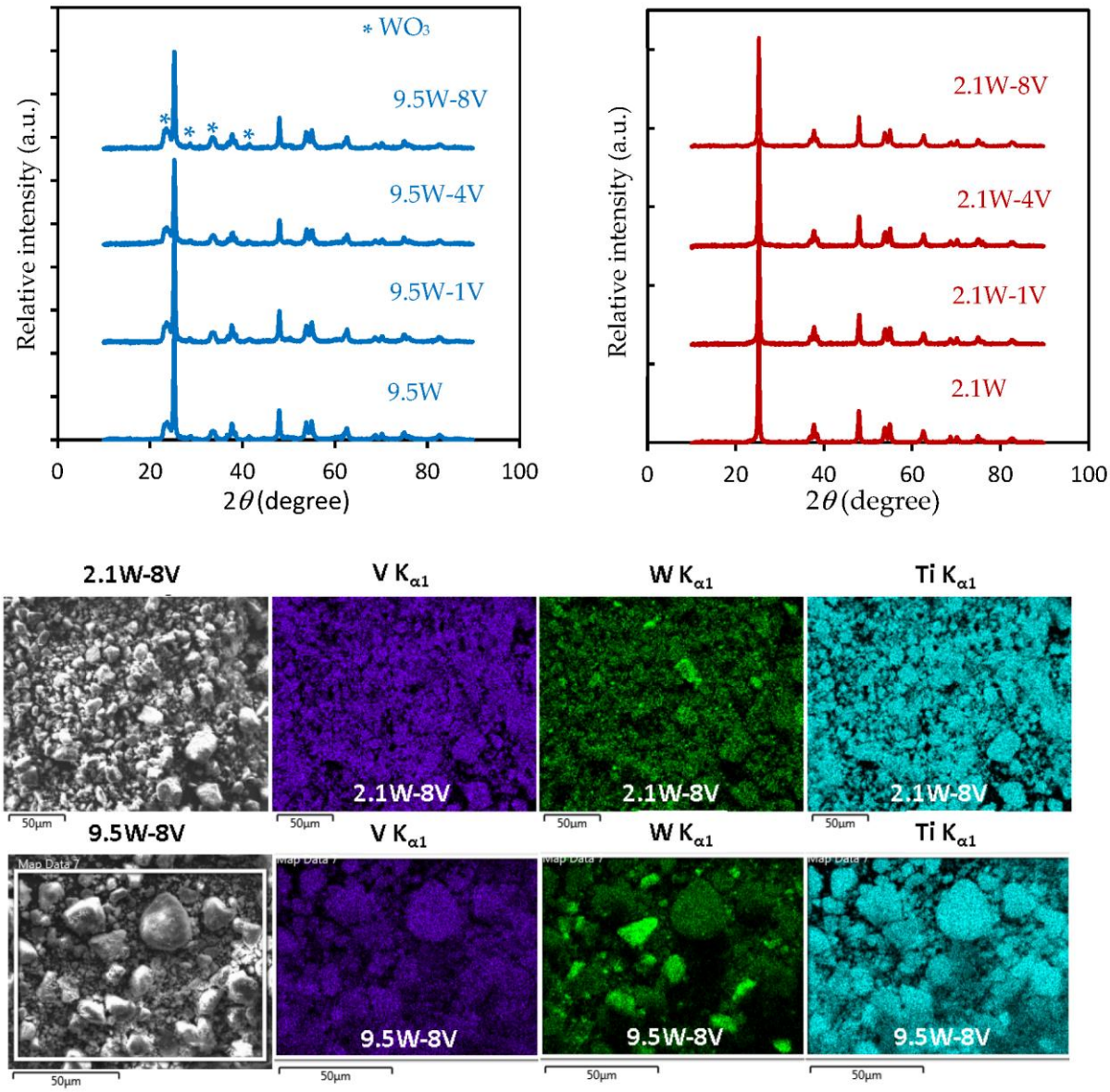

Figure 5. XRD and EDS analyses on freshly prepared V_2O_5-WO_3/TiO_2 catalysts calcined in air at 450 °C.

3.3.2. Raman Spectroscopy

Raman spectra on V_2O_5-WO_3/TiO_2 are collected in Figure 6. They are dominated by the characteristic Raman lines of TiO_2 anatase centered at 392 cm^{-1} (B_{1g}, δ_{TiOTi}), 510 cm^{-1} (A_{1g}, B_{1g}, ν_{TiO}), 628 cm^{-1} (E_g, ν_{TiO}), and broad and weak second-order features at 792 cm^{-1} [23]. A broad and weak line with an apparent maximum near 805 cm^{-1} for 2.1W-xV sample has been tentatively assigned to oxotungstate species [24,25]. In the wavenumber ranges 1000–800 cm^{-1} and 800–600 cm^{-1}, the presence of V=O and V-O-V stretching modes for polyvanadate species can be detected, respectively [26,27]. Nonetheless, the intensification of the 805 cm^{-1} Raman line for 9.5W-xV samples allows for the identification of W-O-W structure in poorly dispersed WO_3 aggregates. Regarding vanadate species, a weak detection is remarkable at low V content. A broad and weak Raman line initially forms near 1010 cm^{-1} and then intensifies at increasing vanadium loading and shifts to higher wavenumber ~1030 cm^{-1}. Such trends would reflect the spectral feature of V=O stretching mode for isolated monovanadate species. Two additional Raman lines at 988 cm^{-1} and 280 cm^{-1}, characteristic of bulk V_2O_5 crystallites [28], develop for 2.1W-8V and 9.5W-8V. These trends reproduce for both series and do not seem markedly sensitive to

the tungsten loading. It is worthwhile to note that two Raman lines appear for 9.5W-xV at 263 cm^{-1} and 327 cm^{-1} and a shoulder at ~707 cm^{-1}, for which hypothetical assignment does not seem easy. Starting from a first finding on WO_3/TiO_2, Ramis et al. [29] pointed out the growth of W-O-M structure in the wavenumber range 200–400 cm^{-1}, in which M could be another metal than W. This assertion seems in agreement with the observation reported in Figure 5 for 2.1W-xV with homogeneous distribution of V and W by considering the development of W-O-Ti structure; however, it could be less obvious for the series 9.5W-xV. Let us note that the discussion could be opened in this latter case regarding the growth of W-O-V structure also characterized by Raman line below 400 cm^{-1} [30]. Nonetheless, subsequent Raman spectroscopic investigations on bulk and supported binary V-W mixed oxides also led to the observation of low-wavenumber Raman lines [31], and the formation of such structure at increasing W loading is consistent with these previous findings. However, spectra cut off below 200 cm^{-1} does not allow to conclude with certainty on this hypothetical structure for V_2O_5-WO_3/TiO_2. Additional data coming from spectral features recorded for $CeV_{1-x}W_xO_4$ [14] open the debates at high W tungsten on the formation of mixed W-O-V compound coexisting with large WO_x aggregates. Indeed, Gillot et al. found on $CeV_{1-x}W_xO_4$ Raman lines at 285 cm^{-1}, 306 cm^{-1}, 702 cm^{-1} and 994 cm^{-1}, which are comparable in terms of location to the band observed for 9.5W-8V, which suggests that the formation of the $TiW_{1-x}V_xO_3$ entity coexisting with WO_x could not be completely ruled out.

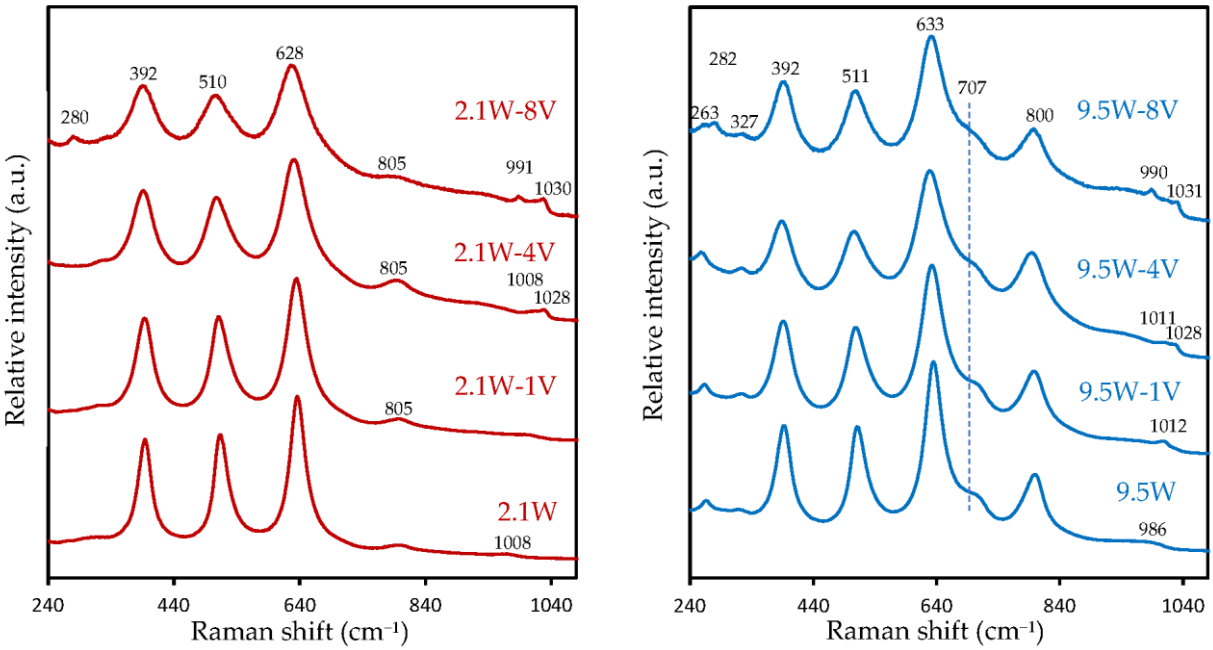

Figure 6. Raman spectra recorded on V_2O_5-WO_3/TiO_2 catalysts calcined in air at 450 °C.

3.3.3. UV-Visible Spectroscopy

UV-visible absorption spectroscopy is a useful technique to probe the electronic structure of the valence bands. For metal oxides, the broad nature of charge transfer does not provide accurate determination of the energy at maximum. For the vanadium undoped samples, the wavelength values determined in Figure 7a agree with those obtained on TiO_2 corresponding to charge transfer from the O 2p valence band to the Ti 3d valence band. The corresponding absorption edge energy values (ΔE) were calculated according to Equation (8), where h is the Planck constant, c is the light celerity and λ is the wavelength values determined from Figure 7a.

$$\Delta E = hc/\lambda \quad (8)$$

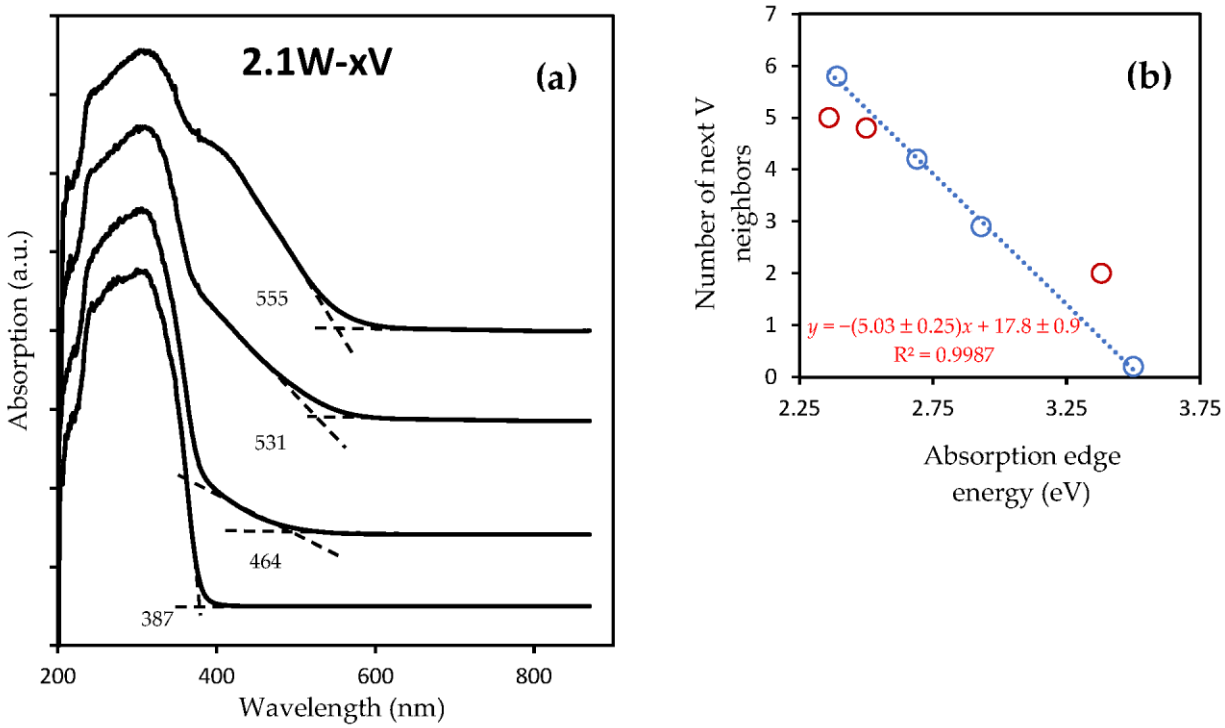

Figure 7. UV-vis spectra recorded for the series 2.1W-*x*V (**a**) and relationship between the estimated absorption edge value from (**a**) and the number of next V neighbors in VO_x clusters (**b**). Red circle data from reference [27], blue circle data from reference [28].

Numerical values for ΔE are reported in Table 5. As seen, V addition induces a decrease of ΔE with a rise of vanadium content, which agrees with previous observations reporting charge transfer transitions in the range 2–4 eV. Previous investigations showed that the energy at the absorption edge can depend on the size of the single metal oxides [32,33]. Data earlier obtained for V_2O_5/Al_2O_3 and for well-defined stoichiometric compounds [27,28] can lead to a linear relationship between ΔE and the number of next vanadium neighbors (see Figure 7b). Based on this linear relationship, extrapolation with calculated ΔE values for 2.1W-*x*V and for 9.5W-*x*V can lead to a rough estimation of the number of next vanadium neighbors. The values reported in Table 5 for a given V density for 2.1W-*x*V and 9.5W-*x*V are comparable and do not reflect a significant impact of tungsten concentration in terms of dilution or contraction effects that would significantly change the size of the VO_x clusters.

Table 5. Textural properties and spectral features extrapolated from UV-vis spectra recorded for V_2O_5-WO_3/TiO_2.

Catalyst	Specific Surf. Area (m^2/g)	Pore Volume (cm^3/g)	V/W	Wave Length λ (nm)	Absorption Edge Energy ΔE (eV)	Number of Next V Neighbors
2.1W	60	0.33	0	387	3.21	
2.1W-1V	59	0.31	0.48	464	2.68	4.3
2.1W-4V	53	0.29	1.90	531	2.34	6.0
2.1W-8V	51	0.27	3.81	555	2.24	6.5
9.5W	52	0.25	0.00	412	3.02	
9.5W-1V	48	0.22	0.11	468	2.66	4.4
9.5W-4V	38	0.20	0.42	531	2.34	6.0
9.5W-8V	34	0.18	0.84	556	2.23	6.5

3.3.4. Bulk Reducibility of VO_x and WO_x Species

Redox properties of ammonia-SCR catalysts are closely related to the redox potential of oxidic tungsten and vanadium species. Their reducibility has been investigated from H_2-Temperature-programmed reduction experiments (H_2-TPR). The consumption profiles are reported in Figure 8 for the two series 2.1W-*x*V and 9.5W-*x*V. The reduction of Ti^{4+} into Ti^{3+} takes place similarly for both series above 500 °C, with a maximum near 630 °C. Regarding the 2.1W-*x*V samples, subsequent addition of W leads to a slight shift of TiO_2 reduction to lower temperature, which reflects a strong interaction between WO_x and TiO_2. Jointly, an extra H_2 consumption is observable in the range 650–900 °C, with two apparent maxima equally reflecting a two-step reduction process of a single oxidic tungsten species and/or the reduction of WO_x species in different chemical environments. Below 600 °C, a reduction process develops, assigned to the reduction of monomeric and polymeric vanadate species. The component in the range 520–530 °C develops at increasing V content but tends to attenuate, reaching the maximum V content corresponding to the formation of less reducible VO_x aggregates. By examining the 9.5W-*x*V, it seems obvious that the reduction of WO_x species dominates even with the observation of two maxima. However, a continuous shift to lower temperature is observable for the low-temperature process. Parallel to this observation, the reduction of VO_x takes place but seems more delayed with the appearance of an extra reduction process near 608 °C. A peculiarity also appears above 950 °C for 9.5W-*x*V with $x = 4$ and 8 with a sharp increase in H_2 consumption. All these observations reflect more complex interactions between tungsten, vanadium and the support, which seems to corroborate previous observations from Raman spectroscopy, possibly related to multiple interactions associated to the growth of V-O-W and W-O-Ti structures. This tentative explanation seems consistent with previous findings for similar catalysts emphasizing a co-reduction of $V^{5+} \rightarrow V^{4+}$ of polymeric surface vanadate species and $W^{6+} \rightarrow W^{4+}$ taking place in the temperature range 510–600 °C [34]. Kompio et al. also provided a comparable explanation for V_2O_5-WO_3/TiO_2 systems [15]. They argued, from H_2-TPR observations, that a faster reduction of V^{5+} occurs when W^{6+} species are the nearest neighbor.

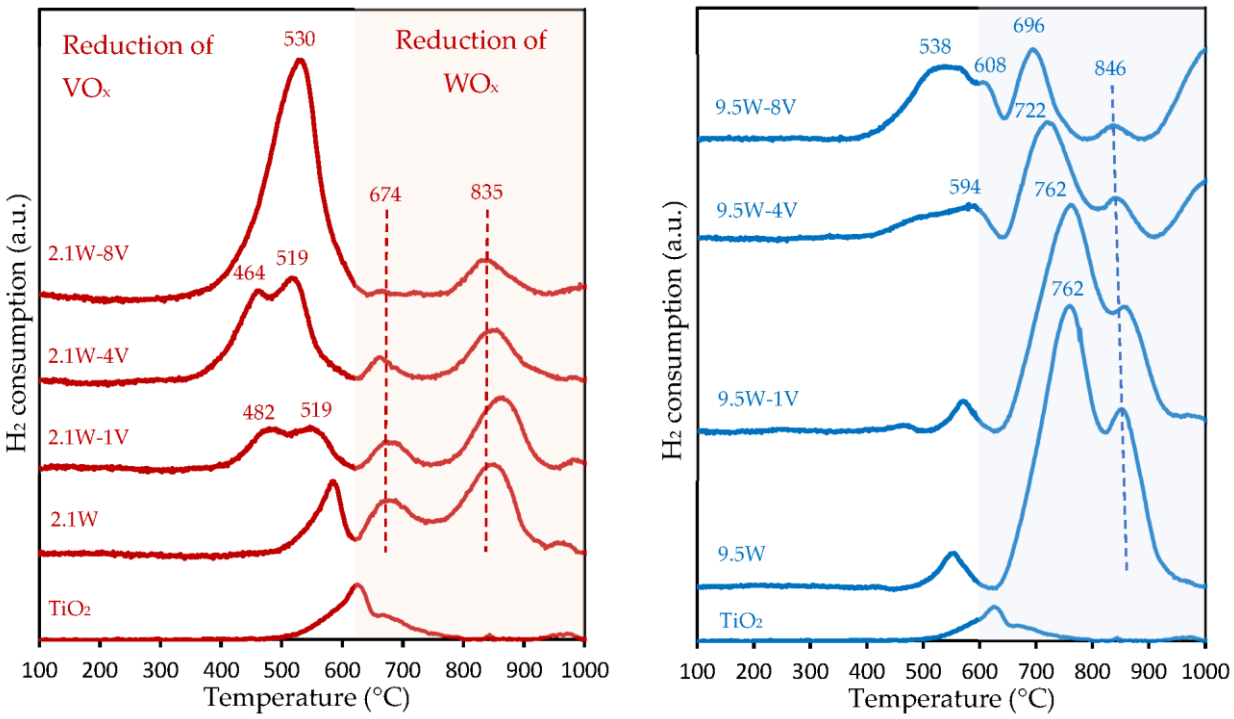

Figure 8. H_2-consumption profiles vs. temperature from H_2-TPR experiments for calcined V_2O_5-WO_3/TiO_2 SCR-catalysts.

3.4. Surface Properties of Supported V_2O_5-WO_3/TiO_2 Catalysts

3.4.1. Textural Properties

Textural properties from nitrogen physisorption measurements at −196 °C are reported in Table 5. Successive impregnations of TiO_2 by tungsten and vanadium induce a gradual loss of specific surface area at increasing loading. Jointly, a moderate contraction effect on the pore volume is noticeable, which does not emphasize a strong pore plugging, in agreement with homogeneous distributions of W and V. Let us note that such tendencies are more pronounced for 9.5W-8V, which could be in connection with a preferential formation of larger WO_x aggregates.

3.4.2. Surface Acidity Probed from Pyridine and Ammonia Adsorption-Desorption Experiments

Regarding pyridine adsorption, infrared spectra were recorded on pre-adsorbed samples at saturation after evacuation under vacuum at 150 °C. Spectra reported in Figure 9 agree with previous assignments. The ring deformation of pyridine is typically observed in the range 1400–1700 cm^{-1}. Infrared bands appearing at 1610 cm^{-1} (ν_{8a}), 1580 (ν_{8b}), 1490 (ν_{19a}) and 1448 cm^{-1} (ν_{19b}) were previously ascribed to the vibrational modes of pyridine adsorbed on Lewis acid sites. Brønsted acid sites lead to the appearance of absorption bands near 1635 cm^{-1} (ν_{8a}) and 1540 (ν_{19b}), characteristic of pyridinium ion in interaction with Brønsted acid sites [35,36]. Figure 9A shows the growth of IR bands near 1535 and 1635 cm^{-1} with a rise in vanadium content. Such a tendency seems less accentuated for the series 9.5W-*x*V because they already appear distinctly on 9.5W. These two IR bands are usually assigned to Brønsted acid sites. Such comparison suggests that the growth of Brønsted acid sites more pronounced on 2.1W-*x*V is related to the accumulation of VO_x at increasing V content. Subsequent increase in temperature favors the desorption of adsorbed pyridine molecules (not shown), revealing different strengths of adsorption, especially a weaker adsorption on Brønsted acid sites. Quantitative exploitation is resumed in Table 6, which confirms the aforementioned observations highlighting a gradual decrease of the Lewis-to-Brønsted ratio on 2.1W-*x*V and 9.5W-*x*V series with increased vanadium content. Comparing the total amount of adsorbed pyridine and normalized uptake, a maximum adsorption capacity appears for $x = 4$. This evolution underlines a detrimental effect of vanadium at high content suppressing strong Lewis acid sites by weaker Brønsted acid sites. In order to obtain more insights into the consequences of this adsorption behavior on the catalytic properties, ammonia adsorption has been investigated thanks to temperature-programmed desorption experiments (NH_3-TPD). NH_3-TPD curves recorded for 2.1W-*x*V are reported in Figure 10. In the absence of vanadium, the decomposition of the overall signal reveals two components with apparent maxima at 300 °C and 424 °C. Subsequent incorporation of vanadium leads to the appearance of a third component at lower temperature ~227 °C for 2.1W-*x*V. At first glance, this one could be assigned to the growth of Brønsted acid sites in agreement with pyridine adsorption. Subsequent addition of vanadium for $x \geq 4$ leads to a significant shift of the overall signal to lower temperature but the intensity signal seems unaffected. The same experiments have been repeated for 9.5W-*x*V samples. Ammonia-TPD profiles reflecting similar features have not been reported. On the other hand, the corresponding ammonia uptakes have been compared in Table 6. Interestingly, V incorporation exerts the same impact on both series, which emphasizes the fact that at low vanadium loading VO_x entities would progressively substitute strong WO_x acid sites with weaker acid sites. Interestingly, for the highest-loaded samples, e.g., 2.1W-8V, and to a lesser extent for 9.5W-8V, an increase in the total amount of desorbed ammonia and in the normalized values is discernible. This trend can be mainly explained by the growth of medium acidic sites.

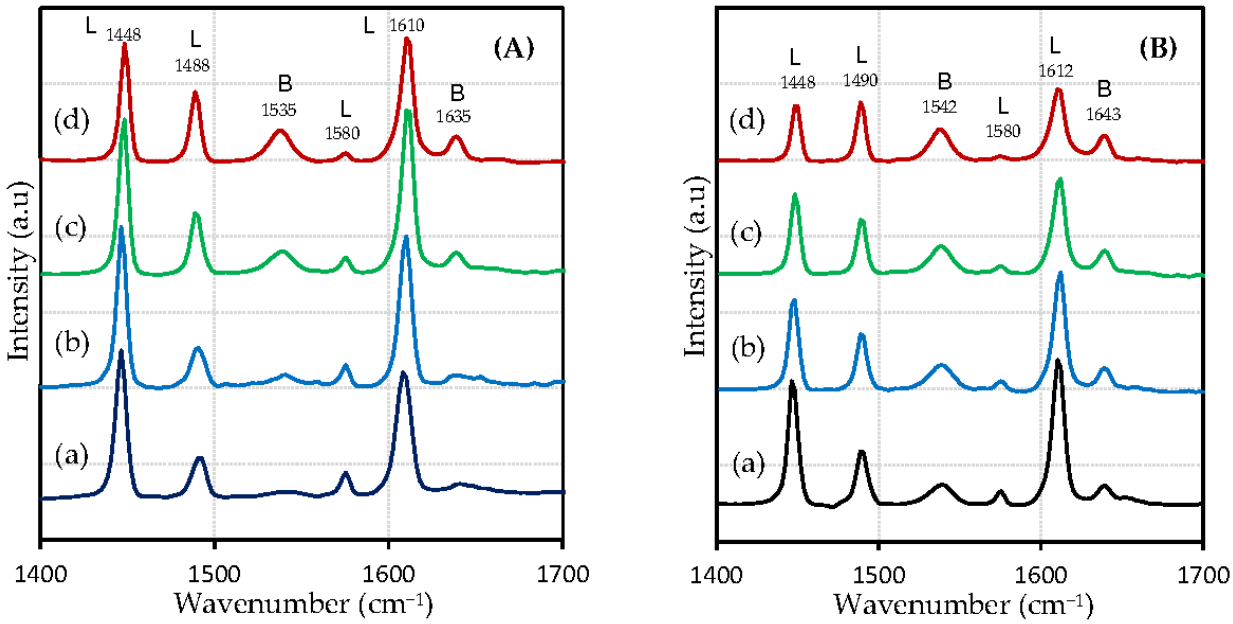

Figure 9. IR spectra recorded for pre-adsorbed pyridine 2.1W-*x*V (**A**) and 9.5W-*x*V (**B**) samples evacuated at 150 °C: *x* = 0 (**a**); *x* = 1 (**b**); *x* = 4 (**c**); *x* = 8 (**d**).

Table 6. Characterization from pyridine and ammonia of acidic site and ammonia adsorption capacity of V_2O_5-WO_3/TiO_2 catalysts.

Catalyst	Pyridine Adsorption at 150 °C			Thermodesorption of Preadsorbed Ammonia				
	Total Adsorbed Amount (μmol.g^{-1})	Normalized Adsorbed Amount [a]	L/B [b]	Total Desorbed Amount (μmol.g^{-1})	Normalized Ammonia Uptake [a]	Weak Ads. [a]	Medium Ads. [a]	Strong Ads. [a]
2.1W	78	1.30	8.3	233	3.89	-	2.35	1.54
2.1W-1V	95.6	1.62	9.1	207	3.51	0.55	1.71	1.25
2.1W-4V	99.6	1.88	2.6	169	3.18	0.60	1.61	0.97
2.1W-8V	87.3	1.71	1.3	197	3.86	0.74	2.27	0.85
9.5W	85.1	1.63	2.3	236	4.54	-	2.14	2.40
9.5W-1V	69.1	1.44	1.4	181	3.76	0.42	1.67	1.67
9.5W-4V	77.2	2.03	1.1	152	4.01	0.80	1.86	1.34
9.5W-8V	58.7	1.73	0.7	152	4.47	0.85	2.81	0.80

[a] expressed in μmol per square meter; [b] Lewis-to-Brønsted acid sites.

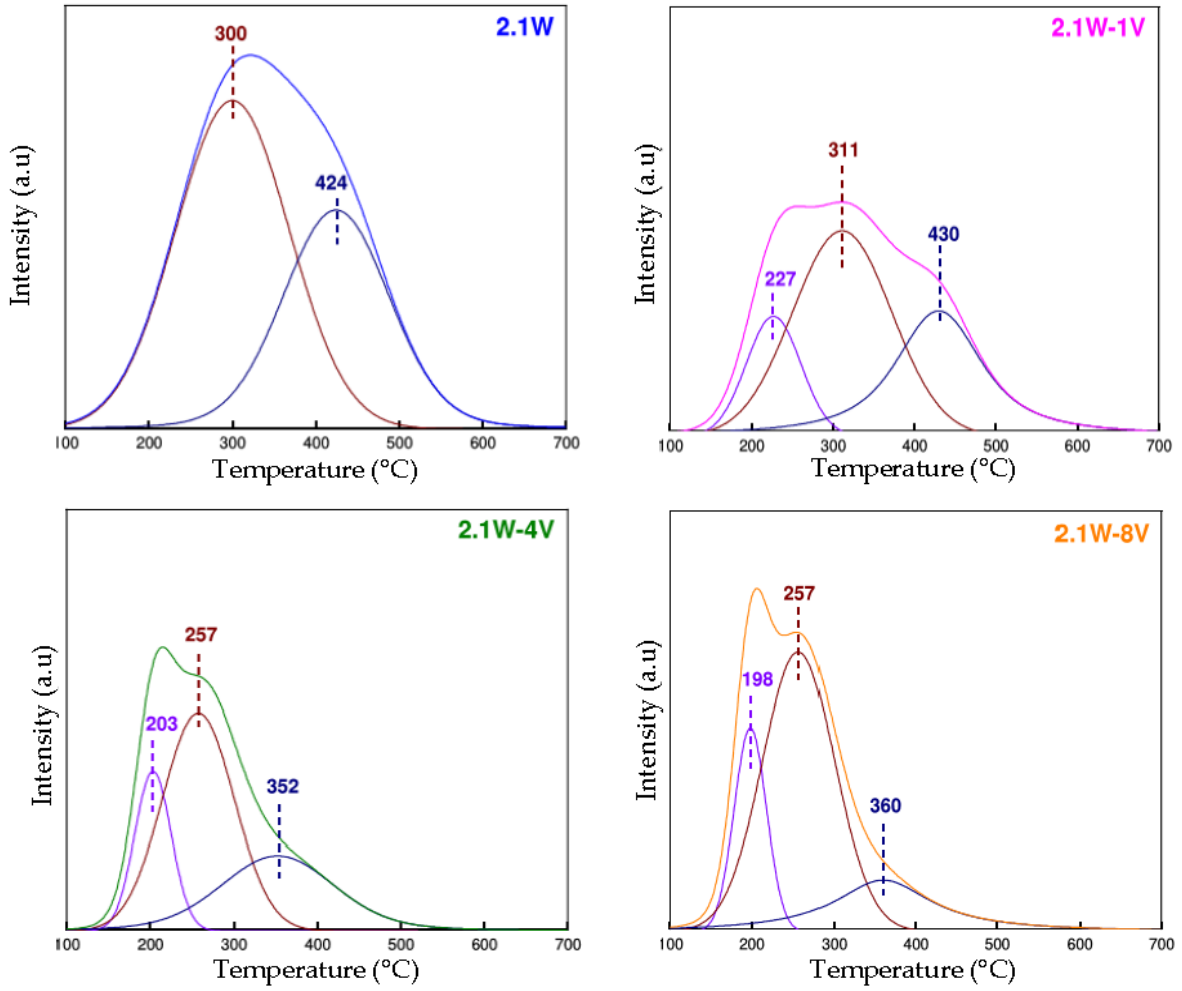

Figure 10. Normalized ammonia-TPD profiles recorded for 2.1W-*x*V: impact of V loading on the acidic functionality.

4. Discussion

Particular attention in this study was paid to the impact of tungsten on the adsorption properties towards ammonia of V_2O_5-WO_3/TiO_2 catalysts and related catalytic properties of active vanadate species in standard SCR conditions. As previously emphasized, numerous studies dealt with the impact of interactions between W and V through electronic or geometric effects, providing renewed fundamental insights into the design of bifunctional sites in association with a pair of V species and/or a combination of surface redox site and an adjacent surface nonreducible metal oxide site [3]. As seen in this study, such interactions vary in their nature according to the V/W ratio. However, the major salient point is undoubtedly related to the impact of water on the catalytic features in terms of activity and selectivity.

Among the two series examined, e.g., 2.1W-*x*V and 9.5W-*x*V, the former does not reflect the typical optimal composition. Indeed, at low W loading, it was expected that W would not exert its expected behavior regarding potential redispersion of VO_x entities and/or preservation of their dispersion. In contrast, this configuration could be more favorable, a priori, to VO_x aggregation, especially at the highest V content. In practice, neither XRD nor Raman spectroscopic measurements reveal a predominant formation of bulk detectable V_2O_5 aggregates. In contrast, homogeneous distribution is observed from SEM-EDS analysis, even at the highest V density for 2.1W-*x*V. UV-vis spectrocopic measurements provide consistent information with absorption edge energy values comparable for 2.1W-*x*V and

9.5W-*x*V, which do not formally emphasize notable dilution or contraction effects at high W content capable of drastically altering the crystallite size distribution of VO_x aggregates.

As a matter of fact, the main difference lies in the characterization of their reducibility. As observed in Figure 8, WO_x and VO_x reduces in different temperature ranges, and subsequent increases in V content do not affect the position and the intensity of the peak reduction of WO_xin 2.1W-*x*V. The most significant changes in this series lie in improved reducibility related to the formation of polyvanadates species at increasing V content. On the other hand, significant changes are noticeable for 9W-*x*V, with improved reducibility of WO_x at increasing V loading and the appearance of an extra reduction process at 608 °C. Such observations can be closely related to the explanation given by Kompio [15], with perturbation induced by the close proximity of W and V associated with a co-reduction. Hence, mixed metal oxide W-O-V cannot be strictly ruled out, especially for 9W-8V, and could reasonably explain the growth of additional Raman lines typical for $x \geq 0.4$. If W seems to exert, a priori, a neutral impact on 2.1W-*x*V, the conjunction of high W and V contents could lead to specific interactions that alter the peculiar reducibility of VO_x and WO_x species. Surface acidic properties from pyridine and ammonia adsorption desorption experiments provide useful information because those observed on 9W-*x*V slightly differ from those obtained on 2.1W-*x*V. First, pyridine adsorption is weakened on 9W-*x*V, with a rise in V content. In contrast, pyridine uptake is enhanced after V incorporation for the series 2.1W-*x*V. However, in both cases, strong Lewis acid sites are progressively replaced by weak Brønsted acid sites with increased vanadium content. These evolutions are in good agreement with ammonia-TPD experiments, which show a continuous decrease in strongly adsorbed ammonia species and, correlatively, the growth of adsorbed ammonia molecules on weak acid sites. Based on this, antagonistic evolutions of the catalytic behavior can be envisioned, associated with a weakening of the storage of ammonia at high temperature, whereas this detrimental effect would be less perceptible, or even suppressed, at low temperature. To a certain extent, this correctly explains the loss of selectivity observed in dry conditions, with the occurrence of competitive ammonia oxidation leading to a loss of NO reduction to nitrogen. Hence, at high temperature, ammonia-SCR would be enhanced at high ammonia coverage according to Equation (9), for which strong ammonia adsorption is a prerequisite.

$$r = k(T)(NO)\theta_{NH_3} \quad (9)$$

Changes in selectivity in wet conditions can be also explained from Equation (9), which means that a strengthening of the ammonia adsorption occurs in the presence of steam. It is obvious that these evolutions cannot be simply explained from pyridine and ammonia adsorption performed in dry conditions. Indeed, the opposite evolutions observed on the surface acid properties are not compatible with the suppression of the undesired ammonia oxidation, to the benefit of the SCR reaction selectively producing nitrogen equally on both series. Probably, these changes in the distribution in the strength of acid sites could be partly explained by the capacity of water to hydrolyze strong Lewis acid sites to strong Brønsted acid sites [17].

Returning to the catalytic behavior at steady-state and low temperature (T = 160 °C), some differences are noticeable in dry and wet conditions, as earlier discussed in Figure 4. According to previous conclusions showing a moderate effect of W in the reconstruction of VO_x species, we have established some comparisons based on the number of nearest-neighbor V atoms in VO_x clusters estimated in Table 5. As seen in Figure 11, the plots of normalized rates expressed per square meter vs. the number of next-neighbor V in VO_x entities leads to different evolutions in dry and wet conditions. Even though the amplitude of variation of the reaction rates is rather limited, the most important observation lies in the opposite trend observed in dry conditions for 2.1W-*x*V and 9.5W-*x*V, while the same evolution is equally observed for 2.1W-*x*V and 9.5W-*x*V in wet conditions, conforming in this later case to a linear relationship (see Figure 11a). As explained, if no comparison seems obvious with adsorption measurements performed in dry conditions, it must be noted that the evolution observed in Figure 11a in wet conditions follows, for both series,

the growth observed on Brønsted acid sites due to the neutralization of strong acid WO_x sites following the addition of vanadium. At first glance, this explanation could be in rather good agreement with a two-site reaction mechanism involving unreactive WO_x species inducing slight structural effects for stabilizing oligomeric -V^{5+}-O-V^{4+} bifunctional sites [16]. In contrast, this explanation seems no longer valid to reconcile the observations in dry conditions reported in Figure 11b. In such cases, subsequent comparisons with physicochemical characterization would be more relevant, and the evolution could be partly explained by the alteration of adsorptive properties of vanadate species by tungsten. As seen on the plot drawn for 9.5W-*x*V, the co-reduction of V^{5+} and W^{6+} could reflect hybrid V-O-W with enhanced acidic properties that cause the gain in performances observed for 9.5W-8V. In the particular case of 2.1W-*x*V, such structure is not detected from H_2-TPR experiments, and the reverse trends observed for 2.1W-8V, with a decrease in the normalized reaction rate, could be more related to a loss of redox properties following the aggregation of VO_x species into unselective VO_x aggregates.

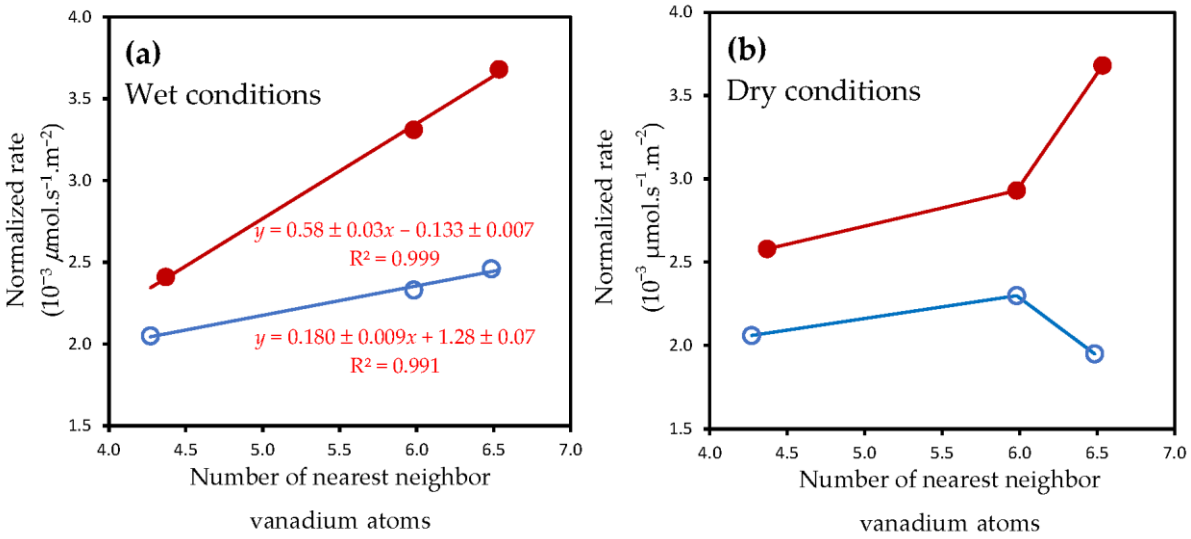

Figure 11. Dependency of the nearest vanadium atoms in VO_x clusters on the normalized reaction rates measured on 2.1W-*x*V (○) and 9.5W-*x*V (●) exposed at 160 °C to 400 ppm NO, 400 ppm NH_3, 8 vol.% O_2 in the presence (**a**) and in the absence of 10 vol.% H_2O (**b**).

5. Conclusions

The effect of tungsten at low (2.1W/nm^2) and high (9.5W/nm^2) surface density on the adsorptive properties and related catalytic properties of active VO_x species has been investigated in dry and wet conditions (with 10 vol.% H_2O). No significant changes were distinctly observed due to aggregation or redispersion of VO_x species according to W content. The sintering of monomeric to polymeric VO_x species up to the formation of V_2O_5 is observed at high V content, irrespective of W content. Pyridine and ammonia adsorption show, for 2.1W-*x*V and 9.5W-*x*V samples, a weakening of acid sites at increasing V content, with the substitution of strong Lewis acid sites by weak Brønsted acid sites. These evolutions agree with the catalytic behavior in dry conditions at high temperature with the appearance on both series of the parasitic ammonia oxidation. On the other hand, this reaction is prevented in the presence of water, suggesting an extra production of strong acid sites in the presence of water.

At low temperature, the catalytic behavior also differs in dry and wet conditions. In the absence of vanadium, water inhibition appears. On the other hand, this detrimental effect tends to disappear after V addition, a slight beneficial effect even appearing on both series, which still emphasizes the fact that the acid properties could still be the driving force at low temperature in wet conditions. A good correlation is observed regarding the

evolution of the normalized reaction rate vs. the next-nearest V neighbor atoms in VO_x clusters, suggesting the involvement of polyvanadates species combining redox and acid properties on 2.1W-*x*V and 9.5W-*x*V. In contrast, some divergences appear in dry conditions as the neutralization of strong acid WO_x sites, jointly to VO_x aggregation 2.1W-*x*V, could be responsible for the decrease in normalized reaction rate at the highest V content. In contrast, the opposite was observed for 9.5W-*x*V, where a rate enhancement seems to be related to preferential interaction between vanadium and tungsten.

Hence, the close interaction between V and W seems to be the driving force both to preserve and enhance catalytic performances in dry conditions. Obviously, the probability to reach this condition is optimal when both elements reach their highest composition. If one condition is not fulfilled, i.e., at low W density, loss of catalytic efficiency occurs. In the presence of steam, there is no discontinuity observed for these two series, with a gradual increase in the reaction rate. Finally, such different behaviors emphasize the critical importance of acidic properties, which outperform redox properties in the definition of the active site, at least in our operating conditions.

Author Contributions: Experimental work data analysis was performed by H.W.S.; conceptualization and interpretation, C.D. and A.M.; supervisor of this work, P.G., interpretation writing of the original article. All authors have read and agreed to the published version of the manuscript.

Funding: The authors would like to thank the Region Hauts de France and ADEME for supporting this work through a Ph.D. grant (H.W.S.). We greatly acknowledge Pardis Simon and Olivier Gardoll, who conducted XPS measurements and thermal analysis.

Data Availability Statement: The data presented in this study are available on request from the corresponding author.

Conflicts of Interest: The authors declare no conflict of interest.

References

1. Dumesic, J.A.; Topsøe, N.-Y.; Topsøe, H.; Chen, Y.; Slabiak, T. Kinetics of Selective Catalytic Reduction of Nitric Oxide by Ammonia over Vanadia/Titania. *J. Catal.* **1996**, *163*, 409–417. [CrossRef]
2. Busca, G.; Lietti, L.; Ramis, G.; Berti, F. Chemical and mechanistic aspects of the selective catalytic reduction of NO_x by ammonia over oxide catalysts: A review. *Appl. Catal.* **1998**, *B18*, 1–36. [CrossRef]
3. Wachs, I.E.; Deo, G.; Weckuysen, B.M.; Andreini, A.; Vuurman, M.A.; de Boer, M.; Amiridis, M.A. Selective Catalytic Reduction of NO with NH_3 over Supported Vanadia Catalysts. *J. Catal.* **1996**, *161*, 211–221. [CrossRef]
4. Chen, J.P.; Yang, R.T. Role of WO_3 in mixed V_2O_5-WO_3/TiO_2 catalysts for selective catalytic reduction of nitric oxide with ammonia. *Appl. Catal. A* **1992**, *80*, 135–148. [CrossRef]
5. Barton, J.; Guillemet, C. Les émissions polluantes des fours de verrerie. In *Le Verre: Science et Technologie*; EDP Science: Les Ulis, France, 2005; pp. 215–216.
6. Guan, B.; Zhan, R.; Lin, H.; Huang, Z. Review of state of the art technologies of selective catalytic reduction of NO_x from diesel engine exhaust. *Appl. Therm. Eng.* **2014**, *66*, 395–414. [CrossRef]
7. Maunula, T.; Viitanen, A.; Kinnunen, T.; Kannaiinen, K. Design of durable vanadium-SCR catalyst systems for heavy-duty diesel applications. *SAE Tech. Pap.* **2013**, *5*, 2013-26-0049.
8. Dahlin, S.; Nilsson, M.; Bäckström, D.; Bergman, S.L.; Bernasek, S.L.; Petterson, L.J. Multivariate analysis of the effect of biodiesel-derived contaminants on V_2O_5-WO_3/TiO_2 SCR catalysts. *Appl. Catal. B* **2016**, *183*, 377–385. [CrossRef]
9. Nova, I.; dall'Acqua, L.; Lietti, L.; Giamello, E.; Forzatti, P. Study of thermal deactivation of a de-NO_x commercial catalyst. *Appl. Catal. B* **2002**, *35*, 31–42. [CrossRef]
10. Madia, G.; Elsener, M.; Koebel, M.; Raimondi, F.; Wokaun, A. Thermal stability of vanadia-tungsta-titania catalysts in the SCR process. *Appl. Catal. B* **2002**, *39*, 181–190. [CrossRef]
11. Alemany, L.J.; Lietti, L.; Ferlazzo, N.; Forzatti, P.; Busca, G.; Giamello, E.; Bregani, F. Reactivity and physicochemical characterization of V_2O_5-WO_3/TiO_2 De-NO_x catalysts. *J. Catal.* **1995**, *155*, 117–130. [CrossRef]
12. Topsøe, Y. Mechanism of the selective catalytic reduction of nitric oxide by ammonia elucidated by in situ on-line fourier transform infrared spectroscopy. *Science* **1994**, *265*, 1217–1219. [CrossRef]
13. Gillot, S.; Tricot, G.; Vezin, H.; Dacquin, J.-P.; Dujardin, C.; Granger, P. Development of stable and efficient $CeVO_4$ systems for the selective reduction of NO_x by ammonia: Structure-activity relationship. *Appl. Catal. B* **2017**, *218*, 338–348. [CrossRef]
14. Gillot, S.; Tricot, G.; Vezin, H.; Dacquin, J.P.; Dujardin, C.; Granger, P. Induced effect of tungsten incorporation on the catalytic properties of $CeVO_4$ systems for the selective reduction of NO_x by ammonia. *Appl. Catal. B* **2018**, *234*, 318–328. [CrossRef]

15. Kompio, P.G.W.A.; Brückner, A.; Hipler, F.; Manoylova, O.; Auer, G.; Mestl, G.; Grünert, W. V_2O_5-WO_3/TiO_2 catalysts under thermal stress: Responses of structure and catalytic behavior in the selective catalytic reduction of NO by NH_3. Appl. *Catal. B* **2017**, *217*, 365–377. [CrossRef]
16. Jaegers, N.R.; Lai, J.-K.; Le, Y.; Walter, E.; Dixon, D.A.; Vasiliu, M.; Chen, Y.; Wang, C.; Hu, M.Y.; Mueller, K.T.; et al. Mechanism by which Tungsten Oxide Promotes the Activity of Supported V_2O_5/TiO_2 Catalysts for NO_x Abatement: Structural Effects Revealed by V-51 MAS NMR Spectroscopy. *Angew. Chem. Int. Edt.* **2019**, *131*, 12739–12746. [CrossRef]
17. Rasmussen, S.B.; Portela, R.; Bazin, P.; Ávila, P.; Bañares, M.A.; Daturi, M. Transient operando study on the NH_3/NH_4^+ interplay in V-SCR monolithic catalysts. *Appl. Catalysis B* **2018**, *224*, 109–115. [CrossRef]
18. Gao, F.; Washton, N.M.; Wang, Y.; Kollár, M.; Szanyi, J.; Peden, C.H.F. Effects of Si/Al ratio on Cu/SSZ-13 NH_3-SCR catalysts: Implications for the active Cu species and the roles of Brønsted acidity. *J. Catal.* **2015**, *331*, 25–38. [CrossRef]
19. Inomata, M.; Miyamoto, A.; Murakami, Y. Mechanism of the Reaction of NO and NH_3, on Vanadium Oxide Catalyst in the Presence of Oxygen under the Dilute Gas Condition. *J. Catal.* **1980**, *62*, 140–148. [CrossRef]
20. Qi, G.; Yang, R.T. Performance and kinetics study for low-temperature SCR of NO with NH_3 over MnO_x–CeO_2 catalyst. *J. Catal.* **2003**, *217*, 434–441. [CrossRef]
21. Usberti, N.; Jablonska, M.; Di Blasi, M.; Forzatti, P.; Lietti, L.; Beretta, A.; Design of a "high-efficiency" NH_3-SCR reactor for stationary applications. A kinetic study of NH_3 oxidation and NH_3-SCR over V-based catalysts. *Appl. Catal. B* **2015**, *179*, 185–195. [CrossRef]
22. Bischoff, K.B. An extension of the general criterion for importance of pore diffusion with chemical reactions. *Chem. Eng. Sci.* **1967**, *22*, 525–530. [CrossRef]
23. Guo, M.; Lis, B.M.; Ford, M.E.; Wachs, I.E. Effect of redox promoters (CeO_x and CuO_x) and surface sulfates on the selective catalytic reduction (SCR) of NO with NH_3 by supported V_2O_5-WO_3/TiO_2 catalysts. *Appl. Catal. B* **2022**, *306*, 121108. [CrossRef]
24. Mamede, A.-S.; Payen, E.; Grange, P.; Poncelet, G.; Ion, A.; Alifanti, M.; Pârvulescu, V.I. Characterization of WO_x/CeO_2 catalysts and their reactivity in the isomerization of hexane. *J. Catal.* **2004**, *223*, 1–12. [CrossRef]
25. Dunn, J.P.; Stregr, H.G., Jr.; Wachs, I.E. Oxidation of sulfur dioxide over supported vanadia catalysts: Molecular structure—reactivity relationships and reaction kinetics. *Catal. Today* **1999**, *51*, 301–318. [CrossRef]
26. Xie, S.; Iglesia, E.; Bell, A.T. Effects of Temperature on the Raman Spectra and Dispersed Oxides. *J. Phys. Chem B* **2001**, *105*, 5144–5152. [CrossRef]
27. Banares, M.A.; Wachs, I.E. Molecular structures of supported metal oxide catalysts under different environments. *J. Raman Spectrosc.* **2002**, *33*, 359–380. [CrossRef]
28. Khodakov, A.; Olthof, B.; Bell, A.T.; Iglesia, E. Oxide Supported MoS_2Catalysts of Unusual Morphology. *J. Catal.* **1999**, *181*, 205–216. [CrossRef]
29. Ramis, G.; Busca, G.; Cristiani, C.; Lietti, L.; Forzatti, P.; Bregani, F. Characterization of tungsta-titania catalysts. *Langmuir* **1992**, *8*, 1744–1749. [CrossRef]
30. Banás, J.; Tomašić, V.; Weselucha-Birczyńska, A.; Najbar, M. Structural sensitivity of NO decomposition over a V-O-W/Ti(Sn)O_2 catalyst. *Catal. Today* **2007**, *119*, 199–203. [CrossRef]
31. Guerrero-Pérez, M.O.; Herrera, M.C.; Malpartida, I.; Larrubia, M.A.; Alemany, L.J.; Banãres, M.A. Operando Raman study of propane oxidation over alumina-supported V–Mo–W–O catalysts. *Catal. Today* **2007**, *126*, 177–183. [CrossRef]
32. Khodakov, A.; Yang, J.; Su, S.; Iglesia, E.; Bell, A.T. Structure and properties of vanadium oxide-zirconia catalysts for propane oxidative dehydrogenation. *J. Catal.* **1988**, *177*, 343–351. [CrossRef]
33. Ferreira, R.S.G.; de Oliviera, P.G.P.; Noronha, F.B. The effect of the nature of vanadium species on benzene total oxidation. *Appl. Catal. B* **2001**, *29*, 275–283. [CrossRef]
34. Aguilar-Romero, M.; Camposeco, R.; Castillo, S.; Marín, J.; Luz, V.R.-G.; García-Serrano, A.; Mejía-Centeno, I. Acidity, surface species, and catalytic activity study on V_2O_5-WO_3/TiO_2 nanotube catalysts for selective NO reduction by NH_3. *Fuel* **2017**, *198*, 123–133. [CrossRef]
35. Hatayama, F.; Ohno, T.; Maruoka, T.; Ono, T.; Miyata, H. Structure and acidity of vanadium oxide layered on titania (anatase and rutile). *J. Chem. Soc. Faraday Trans.* **1991**, *87*, 2629–2633. [CrossRef]
36. Barzetti, T.; Selli, E.; Moscotti, D.; Forni, L. Pyridine and ammonia as probes for FTIR analysis of solid acid catalysts. *J. Chem. Soc. Faraday Trans.* **1996**, *92*, 1401–1407. [CrossRef]